

Sources of longitudinal flow decorrelations in high-energy nuclear collisions

Jiangyong Jia,^{1,2,*} Shengli Huang,¹ Chunjian Zhang,^{3,4,1} and Somadutta Bhatta¹

¹*Department of Chemistry, Stony Brook University, Stony Brook, NY 11794, USA*

²*Physics Department, Brookhaven National Laboratory, Upton, NY 11976, USA*

³*Shanghai Research Center for Theoretical Nuclear Physics, NSFC and Fudan University, Shanghai 200438, China*

⁴*Key Laboratory of Nuclear Physics and Ion-beam Application (MOE),*

and Institute of Modern Physics, Fudan University, Shanghai 200433, China

The longitudinal structure of the quark-gluon plasma (QGP) consists of several components spanning various scales. However, its short-range features are often obscured by final-state non-flow correlations. Here, we introduce a data-driven approach to separate initial state structures from non-flow effects. The longitudinal structure is found having two distinct components: one that reflects the global twisted geometry of the QGP, and another that captures localized fluctuations in rapidity. The characteristics of this second component, contributing to short- and medium-range flow decorrelations, can be quantified by comparing collisions of nuclei with different shapes. This study represents the first successful attempt to disentangle long- and short-range flow decorrelations from non-flow backgrounds, providing new insights into the initial conditions of heavy-ion collisions.

Introduction. High-energy nuclear collisions serve as laboratories for generating and examining the QGP under varied conditions [1]. Understanding the dynamics and properties of this exotic state requires precise control of its initial conditions (IC), including the distributions of colliding nucleons, their constituent partons, the deposition of energy, and the 3D geometric profile. Recent advancements showcased the potential to fine-tune the IC by comparing collision systems with similar masses yet distinct shapes, allowing for precise control over the QGP's initial shape without altering its hydrodynamic response [2–5]. Leveraging ratios of bulk observables, such as the elliptic flow, between these systems facilitates the extraction of valuable information about the IC [6, 7]. Such experimental comparisons, e.g. between $^{238}\text{U}+^{238}\text{U}$ and $^{197}\text{Au}+^{197}\text{Au}$ [8] or $^{96}\text{Ru}+^{96}\text{Ru}$ and $^{96}\text{Zr}+^{96}\text{Zr}$ [3, 9], have indicated strong impacts of nuclear structure on the geometrical properties of the IC, which in turn can be used to constrain the longitudinal profile [10, 11].

Most investigations of the QGP focused on transverse xy profile of the IC near mid-pseudorapidity ($\eta \approx 0$). However, the energy deposition process by the colliding nucleons is inherently non-boost-invariant and fluctuating along η , known as longitudinal fluctuations or decorrelations [12–15]. Consequently, the initial shape of the QGP and its transverse expansion vary with η even within a single collision event. In popular QCD-inspired string models (PYTHIA [16], HIJING [17], AMPT [18]), where nucleons deposit energy in color flux tubes, longitudinal fluctuations arise from variations in the starting positions and lengths of the flux tubes along η [12, 13]. This gives rise to a global geometry that varies smoothly with η as well as local stochastic fluctuations (see Fig. 1).

We illustrate this concept through an analysis of elliptic flow ($V_2 = v_2 e^{2i\Psi}$), which characterizes the elliptical distribution of particles in the xy -plane. The V_2 captures the hydrodynamic response to an elliptically-shaped overlap region, quantified by the eccentricity vec-

tor

$$\mathcal{E}_2 = \varepsilon_2 e^{2i\Phi} \equiv -\frac{\int e(r, \phi) r^2 e^{2i\phi} r dr d\phi}{\int e(r, \phi) r^2 r dr d\phi}, \quad (1)$$

defined from transverse energy density $e(r, \phi)$ at a given η . The longitudinal structure of V_2 is driven by the asymmetrical energy deposition by forward and back-

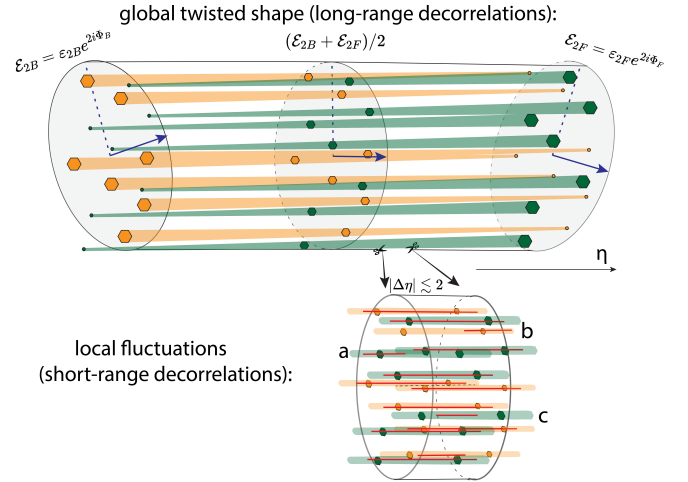


FIG. 1. (top) The initial shape of the QGP has an elliptic component that interpolates between $\mathcal{E}_{2,F}$ at far-forward rapidity and $\mathcal{E}_{2,B}$ at far-backward rapidity, yielding a gradual variation of \mathcal{E}_2 in η . Positions of forward-going (green disks) and backward-going (orange disks) nucleons sweeping out light-colored tubes in which energy may be deposited, where varying tube widths represent asymmetric energy deposition of nucleon, i.e. forward-going nuclei deposit more energy at positive η and vice versa. (bottom) The actual deposited energy from each nucleon spreads over segments (red lines) about $|\Delta\eta| \lesssim 1 - 2$. Within this range (closeby slices), most nucleons deposit energy coherently, but a few may deposit more energy in the left slice (a), right slice (b), or between the two slices (c). This stochastic behavior leads to short-range decorrelations of \mathcal{E}_2 and V_2 .

ward moving participants, resulting in a \mathcal{E}_2 that interpolates between $\mathcal{E}_{2,F}$ and $\mathcal{E}_{2,B}$, the eccentricity vectors defined by the forward-going and backward-going colliding nucleons, respectively [19]. In other words, the initially produced QGP has an elliptic shape that twists and deforms from $\mathcal{E}_{2,F}$ to $\mathcal{E}_{2,B}$, driving a final-state V_2 with a similar η dependence (top of Fig. 1).

Experimentally, elliptic flow is accessed using the two-particle correlation (2PC) method, which quantifies the second moment of its event-by-event distribution,

$$V_{2\Delta}(\eta_1, \eta_2) = \langle V_2(\eta_1) V_2^*(\eta_2) \rangle. \quad (2)$$

The initial state longitudinal fluctuations result in a decrease of $V_{2\Delta}$ for pairs with increasing separation $\Delta\eta = \eta_1 - \eta_2$. Specifically, “global” decorrelations arising from nucleon fluctuations and nuclear deformation lead to gradual variations of $V_{2\Delta}$ with $\Delta\eta$ (the two sources have similar η dependence [11]), whereas “local” decorrelations in energy deposition results in variation of $V_{2\Delta}$ at small $|\Delta\eta|$ (bottom of Fig. 1) [12]. However, the local decorrelations and non-flow are difficult to distinguish, as both appear at relatively small $|\Delta\eta|$. An experimental separation between the initial state short-range correlations and final-state non-flow remains elusive.

In this paper, using correlations between V_2 and different estimates of \mathcal{E}_2 , we identify sources of initial-state-driven decorrelations contributing to $V_{2\Delta}(\eta_1, \eta_2)$. By comparing U+U with Au+Au collisions, we discover a fingerprint of short-range correlation as a dilution of the impact of nuclear deformation, leading to an increase of the ratio of $V_{2\Delta,UU}/V_{2\Delta,AuAu}$ with $\Delta\eta$. We further develop a method to disentangle between long-range correlation, short-range correlation, and final-state non-flow.

Setup. The study is carried out using the transport model, AMPT [18], which simulates the full space-time evolution of heavy-ion collisions event by event. The nucleons are sampled from the Woods-Saxon distribution in polar coordinate: $\rho(r, \theta, \phi) \propto [1 + \exp((r - R_0(1 + \beta Y_{2,0}(\theta, \phi))/a_0))]^{-1}$, where the β is the quadrupole deformation, R_0 is the nuclear radius, and a_0 is the skin thickness. Collisions for three systems are simulated, whose geometrical parameters, listed in Table I, are taken from Ref. [20]. The collision events are generated at $\sqrt{s_{NN}} = 193$ GeV for U+U and $\sqrt{s_{NN}} = 200$ GeV for Au+Au, employing the string-melting mode with a partonic cross-section of 3 mb. Elliptic eccentricities are calculated for all participating nucleons, denoted as \mathcal{E}_2 , as well as for the partons at mid-rapidity $|\eta| < 0.4$ after string melting but before the partonic transport, $\mathcal{E}_{2,quark}$. The partons are weighted by their total energy in the calculation according to Eq. 1, hence $\mathcal{E}_{2,quark}$ captures the initial state local fluctuation associated with strings (Fig. 1) without being impacted by non-flow. The final state particles used for the analysis are chosen from the transverse momentum range $0.2 < p_T < 3$ GeV/c

and pseudorapidity range $|\eta| < 5$. Event centrality is defined by charged particle multiplicity in $|\eta| < 0.5$ (N_{ch}). This analysis focuses on the 0–5% most central collisions, where the impact of nuclear deformation is prominent.

System	$^{238}\text{U}+^{238}\text{U}$	$^{238}\text{U}+^{238}\text{U}$	$^{197}\text{Au}+^{197}\text{Au}$
β	0.28	0.0	-0.14
R_0 (fm)	6.81	6.81	6.62
a_0 (fm)	0.55	0.55	0.52

TABLE I. Nuclei species and their quadrupole deformation β , radius R_0 and skin thickness a_0 used in AMPT simulation.

Elliptic flow is calculated using two different approaches. First, the flow is obtained using the standard 2PC method, $V_{2\Delta}(\eta_1, \eta_2)$, in the pseudorapidity range $|\eta_1|, |\eta_2| < 2$. This is the typical range covered by the detectors at RHIC and the Large Hadron Collider (LHC). The $V_{2\Delta}(\Delta\eta) = \int V_{2\Delta}(\eta, \eta - \Delta\eta) d\eta / \int d\eta$, covering the range $|\Delta\eta| < 4$, captures all the initial-state-driven long-range and short-range correlations illustrated by Fig. 1, as well as final-state non-flow.

In the second approach, we calculate the projection of the flow along the direction of eccentricity vectors,

$$v_{2,\varepsilon}(\eta) \equiv \frac{\langle V_2(\eta) \mathcal{E}_2^* \rangle}{\sqrt{\langle \mathcal{E}_2 \mathcal{E}_2^* \rangle}}, \quad v_{2,\varepsilon_{quark}}(\eta) \equiv \frac{\langle V_2(\eta) \mathcal{E}_{2,quark}^* \rangle}{\sqrt{\langle \mathcal{E}_{2,quark} \mathcal{E}_{2,quark}^* \rangle}} \quad (3)$$

where “ $\langle \rangle$ ” indicates an average over events in a specific centrality range. The $v_{2,\varepsilon}(\eta)$ captures initial-state-driven long-range correlations, while $v_{2,\varepsilon_{quark}}(\eta)$ captures in addition the initial-state-driven short-range correlations. Both observables are free of non-flow. Therefore, comparing the shapes of $v_{2,\varepsilon}^2(\eta)$ and $v_{2,\varepsilon_{quark}}^2(\eta)$ to the shape of $V_{2\Delta}(\Delta\eta)$ facilitates the separation of the initial- and final-state effects.

The values of $V_{2\Delta}$, displayed in Fig. 2(a), decrease gradually with $\Delta\eta$ for all three systems. This decreasing trend is characterized by a mild structure at $|\Delta\eta| < 2$ and a broader one at $|\Delta\eta| > 2$, which as we show later indicates non-flow and initial-state-driven short-range correlations, respectively. The differences

$$V_{2\Delta,\beta}(\Delta\eta) = V_{2\Delta}\{\beta = 0.28\} - V_{2\Delta}\{\beta = 0\} \approx b(\Delta\eta)\beta^2, \quad (4)$$

capture the deformation-driven contribution of Uranium, and has a quadratic dependence on deformation parameter [3, 21]. Based on this discussion, the 2PC flow has four components,

$$V_{2\Delta}(\Delta\eta) = a(\Delta\eta) + b(\Delta\eta)\beta^2 + \text{src}(\Delta\eta) + \text{nf}(\Delta\eta). \quad (5)$$

The $a(\Delta\eta)$ and $\text{src}(\Delta\eta)$ capture the initial-state-driven long-range and short-range correlations in collisions of spherical nuclei, respectively, $b(\Delta\eta)$ has similar long-range structure as $a(\Delta\eta)$ [11], and $\text{nf}(\Delta\eta)$ is associated with non-flow.

Figure 2(b) shows the ratio of $V_{2\Delta}$ between U+U with and without deformation, as well as between U+U and

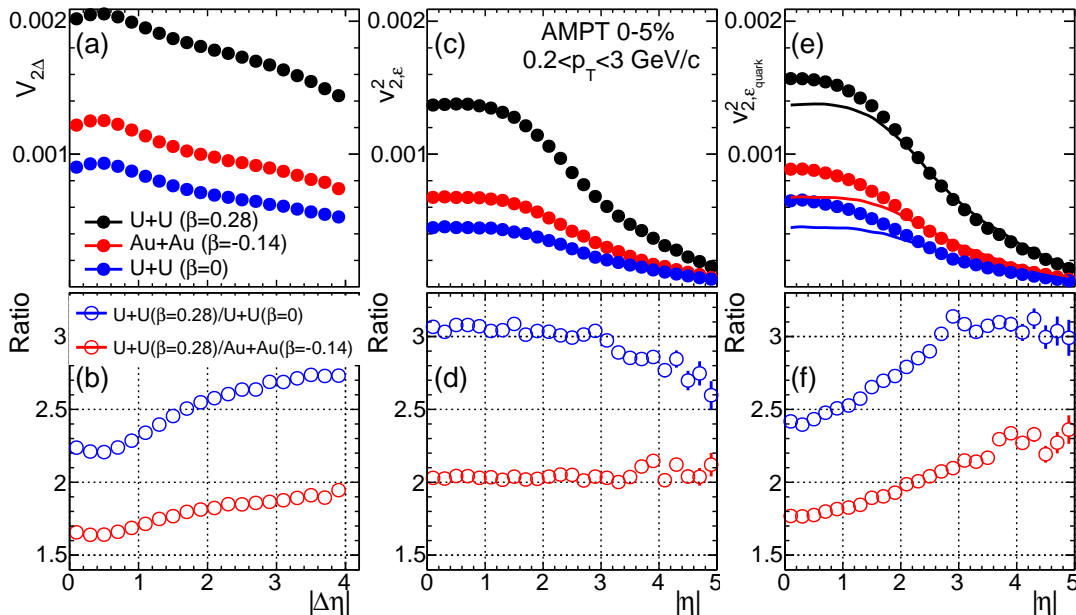


FIG. 2. Elliptic flow calculated using the 2PC method (left), projected to the \mathcal{E}_2 squared (middle), and projected to the $\mathcal{E}_{2,\text{quark}}$ squared (right) in three systems listed in Table I. Bottom panels show the ratios between U+U with and without deformations (open blue circles) and between U+U with deformation and Au+Au (open red circles). The curves in the top-right panel are copies of the data from the middle-top panel, allowing a direct comparison between $v_{2,\epsilon}^2$ and $v_{2,\epsilon}^2_{\text{quark}}$.

Au+Au. The former can be expressed as

$$R_{V_{2\Delta}}(\Delta\eta) = \frac{a(\Delta\eta) + b(\Delta\eta)\beta^2 + \text{src}(\Delta\eta) + \text{nf}(\Delta\eta)}{a(\Delta\eta) + \text{src}(\Delta\eta) + \text{nf}(\Delta\eta)}. \quad (6)$$

Since $\text{src}(\Delta\eta)$ and $\text{nf}(\Delta\eta)$ are short-range, they dilute the impact of nuclear deformation at small $|\Delta\eta|$, leading to an increase of the ratio towards large $|\Delta\eta|$. The increase slows down at $|\Delta\eta| \gtrsim 1.5$, suggesting $\text{src}(\Delta\eta)$ and $\text{nf}(\Delta\eta)$ have different ranges in $\Delta\eta$.

Figure 2(c) and (e) display the results of $v_{2,\epsilon}^2$ and $v_{2,\epsilon_{quark}}^2$ over the full η range. The values are smaller than $V_{2\Delta}$ as expected since they are projections of flow signal and free of non-flow. Their shapes signify the expected η dependence of the single particle flow.

The corresponding ratios between U+U with and without deformation are displayed in the bottom panels. The $R_{v_{2,\epsilon}^2}$ is nearly independent η , which is expected since $v_{2,\epsilon}$ only captures the long-range components a and $b\beta^2$ in Eq. 6, both of which have a similar shape [11]. On the other hand, $R_{v_{2,\epsilon_{quark}}^2}$ displays a gradual increase with η , with a shape that closely resembles Fig. 2(a). Our interpretation is that the local structures of the initial state at mid-rapidity, captured by $\mathcal{E}_{2,\text{quark}}$, generate additional flow around mid-rapidity. This is supported by Fig. 2(e), which shows that $v_{2,\epsilon_{quark}} > v_{2,\epsilon}$ at $|\Delta\eta| < 2$ but they are much closer at $|\Delta\eta| > 2$. The presence of initial state short-range correlation in ϵ_{quark} , contributing to V_2 , is responsible for the gradual increase of $R_{v_{2,\epsilon_{quark}}^2}$ in Fig. 2(f). The bottom panels of Fig. 2 also show ra-

tios between U+U and Au+Au by red circles, which are smaller than ratios between U+U with and without deformation and exhibit weaker $\Delta\eta$ or η dependence as well. This suggests that the impacts of Uranium deformation are partially canceled by the moderate deformation of ^{197}Au .

Clearly, the $\Delta\eta$ dependence of the deformation-driven flow is a reflection of the short-range correlation and its rapidity structure. To quantify the sources of decorrelations in $V_{2\Delta}$, we perform a convolution of $v_{2,\epsilon}(\eta)$ and $v_{2,\epsilon_{quark}}(\eta)$ within $|\eta| < 2$:

$$V_{2\Delta,\epsilon}(\Delta\eta) = \frac{1}{4} \int_{-2}^2 v_{2,\epsilon}(\eta_1) v_{2,\epsilon}(\eta_2) \delta(\eta_1 - \eta_2) d\eta_1 d\eta_2 \quad (7)$$

The expression for $V_{2\Delta,\epsilon_{quark}}(\Delta\eta)$ is analogous. These quantities approximate the initial-state-driven flow decorrelations and can be directly compared to $V_{2\Delta}$.

This comparison is carried out in Fig. 3. The $V_{2\Delta,\epsilon_{quark}}$ has a shape that matches almost perfectly with $V_{2\Delta}$ at $|\Delta\eta| > 2$, while the $V_{2\Delta,\epsilon}$ is much flatter in $|\Delta\eta|$. The shape of $V_{2\Delta,\epsilon}$ is also similar to the shape of $V_{2\Delta,\beta}$ in Eq. 4, suggesting a similarly weak $\Delta\eta$ dependence [11].

These insights enable us to separate components of longitudinal flow decorrelations (shaded areas). The long-range component, $V_{2\Delta,\epsilon}$, dominates, followed by the short-range component induced by local fluctuations. This short-range component starts to decrease at $|\Delta\eta| > 2$, reflecting the typical coherence length of the local fluctuations. The estimated non-flow component, between $V_{2\Delta}$ and $V_{2\Delta,\epsilon_{quark}}$, spans a range of $|\Delta\eta| < 2$.

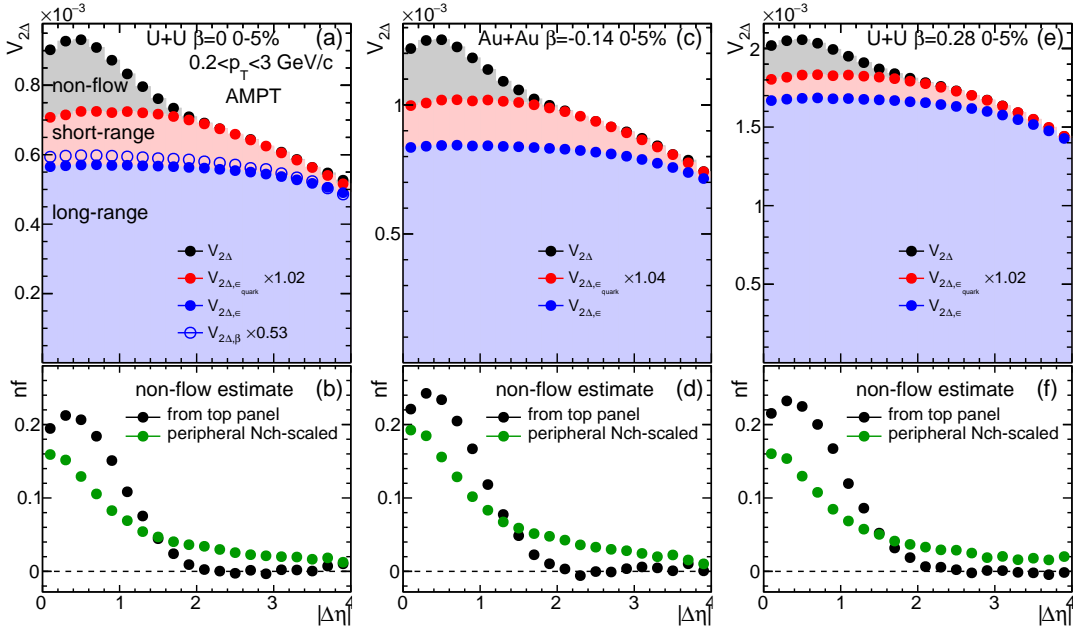


FIG. 3. Top: comparison of $V_{2\Delta}$ (solid black), $V_{2\Delta,\varepsilon_{\text{quark}}}$ (solid red), and $V_{2\Delta,\varepsilon}$ (solid blue) in collisions of undeformed U (a), deformed U (b), and Au (c). A small scale factors are applied so $V_{2\Delta,\varepsilon_{\text{quark}}}$ can match the tail of $V_{2\Delta}$. In panel a, deformation-induced flow $V_{2\Delta,\beta}$ is scaled to match the tail of $V_{2\Delta,\varepsilon}$ (open blue). This comparison allows us to decompose the 2PC $V_{2\Delta}$ in 0-5% most central collisions into a long-range component, a short-range component from the initial state, as well as a non-flow component. Bottom: the estimated non-flow component (solid black) and that estimated from the 90-100% most peripheral collisions selected based on N_{part} , via $V_{2\Delta,\text{nf}} = V_{2\Delta,90-100\%} N_{\text{ch},90-100\%} / N_{\text{ch},0-5\%}$.

Since $V_{2\Delta,\varepsilon_{\text{quark}}}$ may not capture all the initial-state-driven short-range components, this method likely gives an upper-limit of non-flow. In the bottom panels, we compare this component to an estimate obtained by assuming non-flow is unmodified and scales inversely with N_{ch} from Ref. [8]

$$\text{nf}_s(\Delta\eta) = V_{2\Delta,90-100\%} N_{\text{ch},90-100\%} / N_{\text{ch},0-5\%}. \quad (8)$$

Note that 90-100% centrality events are selected based on number of participating nucleons N_{part} , instead of N_{ch} to avoid selection bias. When integrated over $|\Delta\eta| < 2$, the non-flow from the scaling method is about 30-40% lower. The long tail in $\text{nf}_s(\Delta\eta)$, arising mainly from the away-side jet fragmentation, is completely absent in the subtraction method. This is due to jet quenching in AMPT, which is very effective in erasing $\cos(2\Delta\phi)$ component of the away-side at low p_T [22].

Equipped with this knowledge, we are ready to dissect the rising trend of the $R_{V_{2\Delta}}$ in Fig. 2(b). We calculate three ratios between U+U in Fig. 3(a) and Au+Au in Fig. 3(c), $R_{V_{2\Delta}}$, $R_{V_{2\Delta,\varepsilon_{\text{quark}}}}$, and $R_{V_{2\Delta,\varepsilon}}$, and display the results in Fig. 4. According to Eq. 6, the ordering, $R_{V_{2\Delta}} \lesssim R_{V_{2\Delta,\varepsilon_{\text{quark}}}} < R_{V_{2\Delta,\varepsilon}}$, signifies the dilution of the impact of Uranium deformation by non-flow and initial-state short-range correlations. About half of the increase of $R_{V_{2\Delta}}$ is due to non-flow concentrated at $|\Delta\eta| < 2$, while the remaining increase over $2 < |\Delta\eta| < 4$ is due to

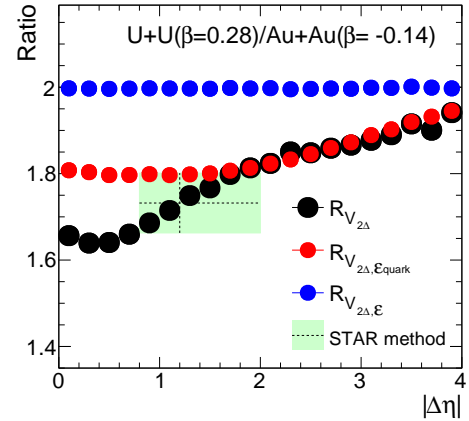


FIG. 4. Ratios of $V_{2\Delta}$ (black), $V_{2\Delta,\varepsilon}$ capturing only the global correlations (blue), and $V_{2\Delta,\varepsilon_{\text{quark}}}$ capturing also initial state short-range correlation (red) between U+U and Au+Au collisions in 0-5% centrality in the AMPT model. They are compared to the corresponding values obtained using the subevent method of STAR [8], corresponding to an average $|\Delta\eta|$ of 1.2 with a 4% uncertainty (green box).

short-range correlations captured by $R_{V_{2\Delta,\varepsilon_{\text{quark}}}}$. These initial-state-driven short-range correlations have a fairly wide range not exhausted even at $\Delta\eta = 4$ where $R_{V_{2\Delta}}$ and $R_{V_{2\Delta,\varepsilon_{\text{quark}}}}$ is still below $R_{V_{2\Delta,\varepsilon}}$. We stress that the impact of short-range correlations and non-flow was re-

vealed only because of the large β_U . Therefore, ratios of isobar or isobar-like systems with different nuclear shapes are excellent tools to explore the rapidity structure of the QGP's initial state.

	fullevent non-flow	subevent non-flow
	$ \Delta\eta < 2$	$0.8 < \Delta\eta < 2$
U+U $\beta = 0.28$	6.9 %	4.2 %
U+U $\beta = 0$	14.4 %	8.7 %
Au+Au $\beta = -0.14$	11.8 %	6.8 %

TABLE II. Estimated non-flow in 0–5% centrality in AMPT within STAR acceptance for full-event and subevent, obtained by integration of the black points in bottom panels of Fig. 3.

Recently, STAR has measured the $R_{V_{2\Delta}}$ between U+U and Au+Au collisions in the range $|\Delta\eta| < 2$, and compared with a hydrodynamic model to constrain the deformation of the Uranium nucleus [8]. The hydrodynamic model includes non-flow from resonance decays but not jets, and has no long-range decorrelation effects. The STAR measurement was performed within the two-subevent method, nearly equivalent to the 2PC method with a cut of $0.8 < |\Delta\eta| < 2$. For this choice, the estimated non-flow in AMPT model is 6.8% for Au+Au collisions (see Table II), reducing to 4% for $R_{V_{2\Delta}}$ between U+U and Au+Au, consistent with the uncertainty quoted by the STAR measurement [8]. Previous estimations rely on multi-parameter fit of $R_{V_{2\Delta}}(\Delta\eta)$ assume that non-flow either has a double-gaussian shape [23] or having no flow decorrelations [24]. Due to the unconstrained nature of these assumptions, the extracted non-flow fraction may vary up to 20% in central Au+Au collisions. Our approach serves as a valuable tool to expose potential limitations of any non-flow estimation methods.

The presence of a significant initial-state-driven short-range correlation impacts the interpretation of the flow decorrelations based on the factorization ratio $r_2(\eta) = \langle V_2(-\eta)V_2^*(\eta_{\text{ref}}) \rangle / \langle V_2(\eta)V_2^*(\eta_{\text{ref}}) \rangle$ [25, 26], where η_{ref} is typically chosen from forward region, e.g. $\eta_{\text{ref}} > 4$ with a gap of at least 2 units from η , e.g. $|\eta| < 2$. However, the initial-state-driven short-range correlations may span a $|\Delta\eta|$ range larger than $|\eta_{\text{ref}} - \eta|$, reducing the values of r_2 . This component is local and stochastic in nature and therefore is expected to cause random fluctuations of amplitude and direction of V_2 [13, 27]. In this sense, $r_2(\Delta\eta)$ can not be interpreted as reflecting just the decorrelations between $-\eta$ and η .

Summary. We show that initial-state-driven longitudinal flow decorrelations have several components with different ranges in $\Delta\eta$. In addition to the usual global long-range component that are nearly independent of $\Delta\eta$, the flow decorrelations has a significant short-range component that is broader than non-flow correlations. This short-range component was shown to dilute the impact of nuclear deformation out to $\Delta\eta = 4$. Our approach provides a new tool to analyze the initial longitudinal

structure and final state response in transport or hydrodynamic models and can be extended to other bulk observables such as triangular flow and p_T fluctuations.

Understanding the longitudinal dynamics of the QGP is the frontier of high-energy nuclear research. The ability to vary the nuclear shape in isobar or isobar-like collisions provides a means to expose these dynamics. Future research should explore such a possibility by leveraging the large acceptance detectors such as ALICE Phase2 upgrade [28] and fixed target program of the SMOG2 at LHCb [29].

This work is supported by DOE Research Grant Number DE-SC0024602.

* Correspond to jiangyong.jia@stonybrook.edu

- [1] Wit Busza, Krishna Rajagopal, and Wilke van der Schee, “Heavy Ion Collisions: The Big Picture, and the Big Questions,” *Ann. Rev. Nucl. Part. Sci.* **68**, 339–376 (2018), [arXiv:1802.04801 \[hep-ph\]](https://arxiv.org/abs/1802.04801).
- [2] Giuliano Giacalone, Jiangyong Jia, and Vittorio Somà, “Accessing the shape of atomic nuclei with relativistic collisions of isobars,” *Phys. Rev. C* **104**, L041903 (2021), [arXiv:2102.08158 \[nucl-th\]](https://arxiv.org/abs/2102.08158).
- [3] Jiangyong Jia and Chunjian Zhang, “Scaling approach to nuclear structure in high-energy heavy-ion collisions,” *Phys. Rev. C* **107**, L021901 (2023), [arXiv:2111.15559 \[nucl-th\]](https://arxiv.org/abs/2111.15559).
- [4] Govert Nijs and Wilke van der Schee, “Inferring nuclear structure from heavy isobar collisions using Trajectum,” *SciPost Phys.* **15**, 041 (2023), [arXiv:2112.13771 \[nucl-th\]](https://arxiv.org/abs/2112.13771).
- [5] Giuliano Giacalone, “Many-body correlations for nuclear physics across scales: from nuclei to quark-gluon plasmas to hadron distributions,” *Eur. Phys. J. A* **59**, 297 (2023), [arXiv:2305.19843 \[nucl-th\]](https://arxiv.org/abs/2305.19843).
- [6] Benjamin Bally *et al.*, “Imaging the initial condition of heavy-ion collisions and nuclear structure across the nuclide chart,” (2022), [arXiv:2209.11042 \[nucl-ex\]](https://arxiv.org/abs/2209.11042).
- [7] Hao-jie Xu, Wenbin Zhao, Hanlin Li, Ying Zhou, Lie-Wen Chen, and Fuqiang Wang, “Probing nuclear structure with mean transverse momentum in relativistic isobar collisions,” *Phys. Rev. C* **108**, L011902 (2023), [arXiv:2111.14812 \[nucl-th\]](https://arxiv.org/abs/2111.14812).
- [8] STAR Collaboration, “Imaging Shapes of Atomic Nuclei in High-Energy Nuclear Collisions,” (2024), [arXiv:2401.06625 \[nucl-ex\]](https://arxiv.org/abs/2401.06625).
- [9] Mohamed Abdallah *et al.* (STAR), “Search for the chiral magnetic effect with isobar collisions at $\sqrt{s_{NN}}=200$ GeV by the STAR Collaboration at the BNL Relativistic Heavy Ion Collider,” *Phys. Rev. C* **105**, 014901 (2022), [arXiv:2109.00131 \[nucl-ex\]](https://arxiv.org/abs/2109.00131).
- [10] Somadutta Bhatta, Chunjian Zhang, and Jiangyong Jia, “Energy dependence of heavy-ion initial condition in isobar collisions,” (2023), [arXiv:2301.01294 \[nucl-th\]](https://arxiv.org/abs/2301.01294).
- [11] Chunjian Zhang, Shengli Huang, and Jiangyong Jia, “Longitudinal Structure of Quark-Gluon Plasma Unveiled Through Nuclear Deformations,” (2024), [arXiv:2405.08749 \[nucl-th\]](https://arxiv.org/abs/2405.08749).
- [12] Piotr Bozek and Wojciech Broniowski, “The torque effect and fluctuations of entropy deposition in rapidity in

- ultra-relativistic nuclear collisions,” *Phys. Lett. B* **752**, 206–211 (2016), [arXiv:1506.02817 \[nucl-th\]](#).
- [13] Long-Gang Pang, Hannah Petersen, Guang-You Qin, Victor Roy, and Xin-Nian Wang, “Decorrelation of anisotropic flow along the longitudinal direction,” *Eur. Phys. J. A* **52**, 97 (2016), [arXiv:1511.04131 \[nucl-th\]](#).
- [14] Hui Li and Li Yan, “Pseudorapidity dependent hydrodynamic response in heavy-ion collisions,” *Phys. Lett. B* **802**, 135248 (2020), [arXiv:1907.10854 \[nucl-th\]](#).
- [15] Rodrigo Franco and Matthew Luzum, “Rapidity-dependent eccentricity scaling in relativistic heavy-ion collisions,” *Phys. Lett. B* **806**, 135518 (2020), [arXiv:1910.14598 \[nucl-th\]](#).
- [16] Torbjörn Sjöstrand, “The PYTHIA Event Generator: Past, Present and Future,” *Comput. Phys. Commun.* **246**, 106910 (2020), [arXiv:1907.09874 \[hep-ph\]](#).
- [17] Miklos Gyulassy and Xin-Nian Wang, “HIJING 1.0: A Monte Carlo program for parton and particle production in high-energy hadronic and nuclear collisions,” *Comput. Phys. Commun.* **83**, 307 (1994), [arXiv:nucl-th/9502021](#).
- [18] Zi-Wei Lin, Che Ming Ko, Bao-An Li, Bin Zhang, and Subrata Pal, “A Multi-phase transport model for relativistic heavy ion collisions,” *Phys. Rev. C* **72**, 064901 (2005), [arXiv:nucl-th/0411110](#).
- [19] Jiangyong Jia and Peng Huo, “Forward-backward eccentricity and participant-plane angle fluctuations and their influences on longitudinal dynamics of collective flow,” *Phys. Rev. C* **90**, 034915 (2014), [arXiv:1403.6077 \[nucl-th\]](#).
- [20] Wouter Ryssens, Giuliano Giacalone, Björn Schenke, and Chun Shen, “Evidence of Hexadecapole Deformation in Uranium-238 at the Relativistic Heavy Ion Collider,” *Phys. Rev. Lett.* **130**, 212302 (2023), [arXiv:2302.13617 \[nucl-th\]](#).
- [21] Jiangyong Jia, “Shape of atomic nuclei in heavy ion collisions,” *Phys. Rev. C* **105**, 014905 (2022), [arXiv:2106.08768 \[nucl-th\]](#).
- [22] Away-side non-flow shape at low p_T is very broad and dominated by $\cos(\Delta\phi)$ driven by momentum conservation, which is the only harmonics surviving after medium effects.
- [23] M. I. Abdulhamid *et al.* (STAR), “Estimate of background baseline and upper limit on the chiral magnetic effect in isobar collisions at $\sqrt{s_{NN}}=200$ GeV at the BNL Relativistic Heavy Ion Collider,” *Phys. Rev. C* **110**, 014905 (2024), [arXiv:2310.13096 \[nucl-ex\]](#).
- [24] N. M. Abdelwahab *et al.* (STAR), “Isolation of Flow and Nonflow Correlations by Two- and Four-Particle Cumulant Measurements of Azimuthal Harmonics in $\sqrt{s_{NN}} = 200$ GeV Au+Au Collisions,” *Phys. Lett. B* **745**, 40–47 (2015), [arXiv:1409.2043 \[nucl-ex\]](#).
- [25] Vardan Khachatryan *et al.* (CMS), “Evidence for transverse momentum and pseudorapidity dependent event plane fluctuations in PbPb and pPb collisions,” *Phys. Rev. C* **92**, 034911 (2015), [arXiv:1503.01692 \[nucl-ex\]](#).
- [26] Morad Aaboud *et al.* (ATLAS), “Measurement of longitudinal flow decorrelations in Pb+Pb collisions at $\sqrt{s_{NN}} = 2.76$ and 5.02 TeV with the ATLAS detector,” *Eur. Phys. J. C* **78**, 142 (2018), [arXiv:1709.02301 \[nucl-ex\]](#).
- [27] Zhiwan Xu, Xiatong Wu, Caleb Sword, Gang Wang, Sergei A. Voloshin, and Huan Zhong Huang, “Flow-plane decorrelations in heavy-ion collisions with multiple-plane cumulants,” *Phys. Rev. C* **105**, 024902 (2022), [arXiv:2012.06689 \[nucl-ex\]](#).
- [28] Shreyasi Acharya *et al.* (ALICE), “ALICE upgrades during the LHC Long Shutdown 2,” *JINST* **19**, P05062 (2024), [arXiv:2302.01238 \[physics.ins-det\]](#).
- [29] LHCb Collaboration, “LHCb SMOG Upgrade,” [CERN-LHCC-2019-005](#), [LHCb-TDR-020 10.17181/CERN.SAQC.EOWH](#).